

Computational design of armored nanodroplets as nanocarriers for encapsulation and release under flow conditions

François Sicard^{1,2*} and Jhoan Toro-Mendoza³

¹ *Department of Physics and Astronomy, University College London, WC1E 6BT London, UK*

² *Department of Chemical Engineering, University College London, WC1E 7JE London, UK and*

³ *Centro de Estudios Interdisciplinarios de la Física, Instituto Venezolano de Investigaciones Científicas, Caracas 1020A, Venezuela*

Nanocarriers are nanosized materials commonly used for targeted-oriented delivery of active compounds, including antimicrobials and small-molecular drugs. They equally represent fundamental and engineering challenges since sophisticated nanocarriers must show adequate structure, stability, and function in complex ambients. Here, we report on the computational design of a distinctive class of nanocarriers, built from buckled armored nanodroplets, able to selectively encapsulate or release a probe load under specific flow conditions. Mesoscopic simulations offer detailed insight into the interplay between the characteristics of laden surface coverage and evolution of the droplet morphology. First, we describe in detail the formation of *pocket-like* structures in Pickering emulsion nanodroplets and their stability under external flow. Then we use that knowledge to test the capacity of these emulsion-based pockets to yield flow-assisted encapsulation or expulsion of a probe load. Finally, the rheological properties of our model carrier are put into perspective with those of delivery systems employed in pharmaceutical and cosmetic technology.

Over the last decade, special attention has been assigned to the design, characterization, and development of nanocarrier systems, which can have potential in targeted-oriented active molecule delivery. They offer remarkable advantages in a wide range of industrial and medical applications, including food [1], cosmetic [2] and pharmaceutical industries [3]. In this context, nanoparticle-stabilized emulsions, aka Pickering emulsions [4], have been intensively used as drug-delivery vehicles in topical medication [5], where their surfactant-free character makes them attractive for different applications since surfactants often produce adverse effects, such as irritation and haemolytic disturbances [6, 7]. They can also serve as ideal compartments for reactions catalyzed by nanoparticles (NPs) attached at the oil-water interfaces [8–10] and can be used in bacterial recognition technologies. [11, 12] Another important and useful advantage of Pickering emulsions over conventional surfactant-stabilized systems is their enhanced stabilization against coalescence [13] and their smaller environmental footprint [14]. While tremendous progress has been made in particle-based microfluidic technology [15, 16], the characteristics of Pickering emulsions pose a number of intriguing physical questions, including a thorough understanding of the perennial lack of detail about how particles arrange at the liquid/liquid interface. Predicting and controlling this interfacial arrangement is even more challenging under flow conditions.

Here, we report on the computational design of a new class of nanocarriers built from Pickering nano-emulsions, which exhibit a *pocket-like* morphology able

to encapsulate or release a probe load under specific flow conditions. Dissipative Particle Dynamics (DPD) is employed as a mesoscopic simulation method [17] with two aims: (1) to describe in detail the formation of *pocket-like* structures in Pickering nanodroplets and their stability under specific flow conditions and then (2) to test the capacity of the formed pockets to encapsulate or release a probe load. Also, the physical properties of our model carrier are put into perspective within the conditions encountered in the high-shear regime of spreading topical medication on the skin and the transport of targeted carriers in pathological alterations of the vascular system. Despite technological advances in experimental methods to control NP assembly at fluid interfaces [18, 19], the inherent limitation in experimental resolution eludes direct access to local observables, such as the particles' three-phase contact angle distribution and the details of the particles' interfacial network [20] presenting complex geometries, while these pieces of information can be accessed by numerical simulations [13, 21–23].

Water nanodroplets coated with spherical NPs with different diameters and immersed in an organic solvent are considered. The coating is formed by Janus NPs (particles whose surface shows two distinct wetting properties) [24, 25] whose initial three-phase contact angles result in maximum adsorption energy at the fluid-fluid interface [26]. Hence, we are able to quantify the role played by homogeneous and heterogenous NP surface coverage at the emulsion droplet interface when the volume of the droplet is reduced. In particular, we observe in detail the formation of crater-like depressions with selective geometry, which can structurally favour the loading of a probe load. The flow conditions clearly affect the dynamical response of the *pocket-like* armored nanodroplets. Under specific conditions, we observe the

*Corresponding author: francois.sicard@free.fr.

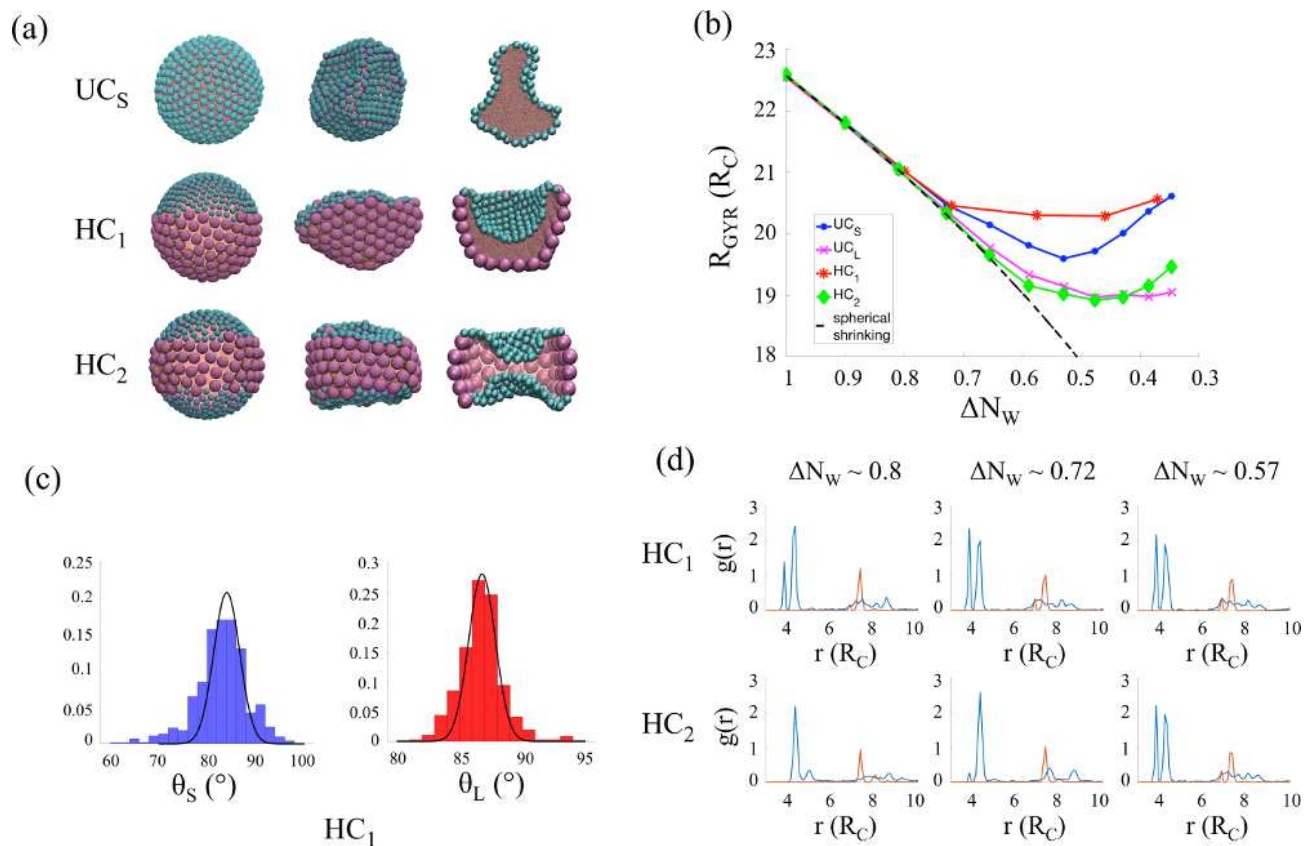


FIG. 1: **Formation of pocket-like structures.** (a) Simulation snapshots representing the initial (left) and final (center) water in oil droplets armored with different nanoparticles surface coverages, obtained from the evaporation process: uniformly covered droplet with small NPs (UC_L) and heterogeneously covered droplets with either each hemisphere covered with small or large NPs (HC_1) or three distinct layers made of small-large-small NPs (HC_2). The cross-sectional view of each system is also shown (right). Cyan and purple spheres represent the small and large Janus NPs, respectively. The detailed structure of the NPs is shown in Fig. S1a in the SI. Pink spheres represent water beads. The oil molecules surrounding the system are not shown for clarity. (b) Evolution of the radius of gyration, R_{GYR} , of UC_S , UC_L , HC_1 , and HC_2 , as a function of the dimensionless parameter $\Delta N_W = N_W/N_W^{(0)}$. N_W represent the number of water beads that remain in the droplet after each removal and $N_W^{(0)}$ is the initial number of water beads. The statistical errors are estimated as one standard deviation from the average obtained for equilibrated trajectories and are always smaller than the symbols. The dashed lines represents the spherical-shrinking regime defined as $R_{GYR} \sim (\Delta N_W)^{1/3}$. (c) Three-phase contact angle distribution of small (blue) and large (red) NPs for HC_1 after the last pumping/equilibration iteration ($\Delta N_W \sim 0.35$). (d) Evolution of the radial distribution function, $g(r)$, with r the distance between the center of the NPs, of small (blue) and large (red) NPs for HC_1 (b) and HC_2 (c).

formation of long-lived anisotropic structures, characteristic of a jammed particle coverage at the liquid-liquid interface. Furthermore, we examine the capacity of the system to control the flow-assisted encapsulation or release of a probe load, which depends on the interplay between NP surface coverage, the level of buckling, and the shear flow conditions.

System characteristics. In Fig. 1a we show representative snapshots of water emulsion nanodroplets in organic solvent (decane) stabilized with Janus NPs. The scaled temperature in the DPD framework is equivalent to 298.73 K. The details of the numerical parametrization and NP structures are given in the Methods section and the Supporting Information (SI). The configurations differ by the size of the NPs and the characteristics of

the surface coverage. We consider small (S) and large (L) NPs with diameters $d_S \sim 2.2$ nm and $d_L \sim 4.5$ nm, whose diffusion coefficients measured on a planar decane/water interface are $D_S \sim 4.7 \pm 3.1 \times 10^{-7}$ cm² s⁻¹ and $D_L \sim 1.8 \pm 0.7 \times 10^{-7}$ cm² s⁻¹, respectively (see Methods and Fig. S1c in the SI). The NPs are originally located at the surface of the emulsion nanodroplets of diameter $d_D \sim 45$ nm. Similar NP surface coverage $\phi \sim 0.8$, as defined in Ref [21, 27], is considered on the armored nanodroplets. This yields similar initial three-phase contact angles $\theta_S \sim 84.1^\circ \pm 2.7^\circ$ and $\theta_L \sim 86.8^\circ \pm 1.1^\circ$ for the small and large NPs, respectively (see Methods and Fig. S1b in the SI), in qualitative agreement with simulations [13, 28, 29] and experimental observations [30]. From the error bars estimated, it is observed that the small NPs are

more sensitive to thermal fluctuations at the interface compared to the large ones, characteristic of the increase of the adsorption energy with the particle radius [31–33]. We also measure the decrease of the interfacial tension, $\Delta\gamma_S$ and $\Delta\gamma_L$, for small and large NPs at planar interfaces for similar NP surface coverage (see Methods). We obtain $\Delta\gamma_S = \gamma_0 - \gamma_S \sim 5.1 \text{ mN.m}^{-1}$ and $\Delta\gamma_B = \gamma_0 - \gamma_B \sim 2.2 \text{ mN.m}^{-1}$, with $\gamma_0 \sim 51.7 \text{ mN.m}^{-1}$ the interfacial tension for a planar decane/water interface [23, 29], and $\gamma_{S,B}$ the interfacial tension when the interface is covered with small or large NPs, respectively. In particular, large NPs have less effect on the reduction of the interfacial tension and are less diffusive than smaller ones, in qualitative agreement with simulations [33] and experimental observations [34]. A lower mobility along with the size of the NPs, will play a key role in the pocket formation.

Formation of pocket-like structures. The volume of the droplets is systematically reduced, by iteratively pumping a small constant proportion of water molecules out of the droplets and letting the systems equilibrate between each iteration, until the systems present dimples and cups at the droplet interface followed by the formation of crater-like depressions, characteristic of the buckling instability [21, 35, 36] (see details in the SI). This process is physically equivalent to a process of solubilization of the dispersed phase into the solvent [21, 35]. We arbitrarily stop the pumping when the number of water molecule constituting the droplets reaches the value $\Delta N_W = N_W/N_W^{(0)} \sim 0.35$, where $N_W^{(0)}$ and N_W are the initial number of water beads and the number of water beads remaining in the droplets, respectively.

In Fig. 1b, we show the evolution of the radius of gyration of the emulsion nanodroplets, R_{GYR} , as a function of the dimensionless parameter ΔN_W . We initially consider spherical droplets whose surface is either uniformly covered (UC) with NPs of identical diameter or heterogeneously covered (HC) with NPs of different diameters. In particular, UC_S (respectively UC_L) is solely covered with small (respectively large) NPs, as shown in Fig. 1a. HC_1 and HC_2 have each hemisphere covered with small and large NPs, or three distinct layers made of small-large-small NPs, respectively (cf. Fig. 1a). When $\Delta N_W > 0.75$, the radii of gyration of four systems follow similar evolution, regardless the NP coverage (UC or HC), characteristic of a spherical-shrinking regime, $R_{\text{GYR}} \sim (\Delta N_W)^{1/3}$ (dashed line in Fig. 1b). When $\Delta N_W < 0.75$, the systems follow different transitions from spherical shrinking to buckling, depending on the characteristics of the NP interfacial packing originating from the difference in surface coverage [37]. This transition happens when the NP monolayer becomes close to its maximum packing, as observed with the evolution of the radial distribution function $g(r)$, with r the distance between the center of the NPs, shown in Fig. 1d and Figs. S2 in the SI. In particular, UC_S and UC_L show different morphological evolutions when

ΔN_W		UC_S	UC_L	HC_1	HC_2
1.0	(S)	$84.1^\circ \pm 2.7^\circ$	–	$84.1^\circ \pm 2.7^\circ$	$84.1^\circ \pm 2.7^\circ$
	(L)	–	86.8 ± 1.1	$86.8^\circ \pm 1.1^\circ$	$86.8^\circ \pm 1.1^\circ$
0.35	(S)	$82.9^\circ \pm 5.9^\circ$	–	$82.8^\circ \pm 6.0^\circ$	82.4 ± 6.4
	(L)	–	$83.6^\circ \pm 9.9^\circ$	$86.7^\circ \pm 1.9^\circ$	87.0 ± 1.8

TABLE I: Measure of the mean (μ) and standard error (σ) of the three phase contact angle distribution in UC and HC droplets in the initial ($\Delta N_W \sim 1.0$) and final ($\Delta N_W \sim 0.35$) configurations.

ΔN_W decreases, with UC_S entering the buckling regime at larger ΔN_W than UC_L , in qualitative agreement with the numerical work of Gu et al. [36]. Finally, below $\Delta N_W \sim 0.45$. R_{GYR} increases as the droplets can be described as half-sphered.

The structures of the armored nanodroplets obtained after the last pumping/equilibration iteration are shown in Fig. 1a (central panel). Visual inspection shows different folding morphologies, depending on the characteristics of the NP coverage. Unlike UC where crater-like depressions form evenly at the interface when the droplet is subject to a compressive surface stress, we observe the formation of well-localised crater-like depressions when the droplet is heterogeneously covered (HC_1 or HC_2), depending on the localisation of the interfacial areas covered with small or large NPs. Notably, we observe the crater-like depressions form in the interfacial areas covered with the smallest NPs, where maximum packing of the interfacial network is achieved quicker and the interfacial tension is lower than those measured for larger NPs.

The properties of the interfacial layers are quantitatively assess via the analysis of the distribution of the three phase contact angles, $\theta_C^{(S)}$ and $\theta_C^{(L)}$, of small and large NPs, respectively. As shown in Fig. S1b in the SI, $\theta_C^{(S)}$ and $\theta_C^{(L)}$ follow Gaussian distributions in the initial configurations ($\Delta N_W \sim 1$), where the shape of the droplets is spherical. When the volume of UC_S and UC_L is reduced, $\theta_C^{(S)}$ and $\theta_C^{(L)}$ uniformly evolve from Gaussian to skewed unimodal distributions, in line with previous work [21]. The values of the respective means, μ_S and μ_L , and standard deviations, σ_S and σ_L , for small and large NPs, respectively, are shown in Table I. Whereas the contact angle distributions show a single peak centered at the same value as the one measured for the initial configuration, σ_S and σ_L show significant variations when the volume of the droplets is reduced, characteristic of the skewness of the distribution and the decrease of the NP–NP distance (cf. Fig. S2 in the SI). When the volume of HC_1 and HC_2 is reduced, on the other hand, we observe significant differences in the evolution of the distributions of $\theta_C^{(S)}$ and $\theta_C^{(L)}$, due

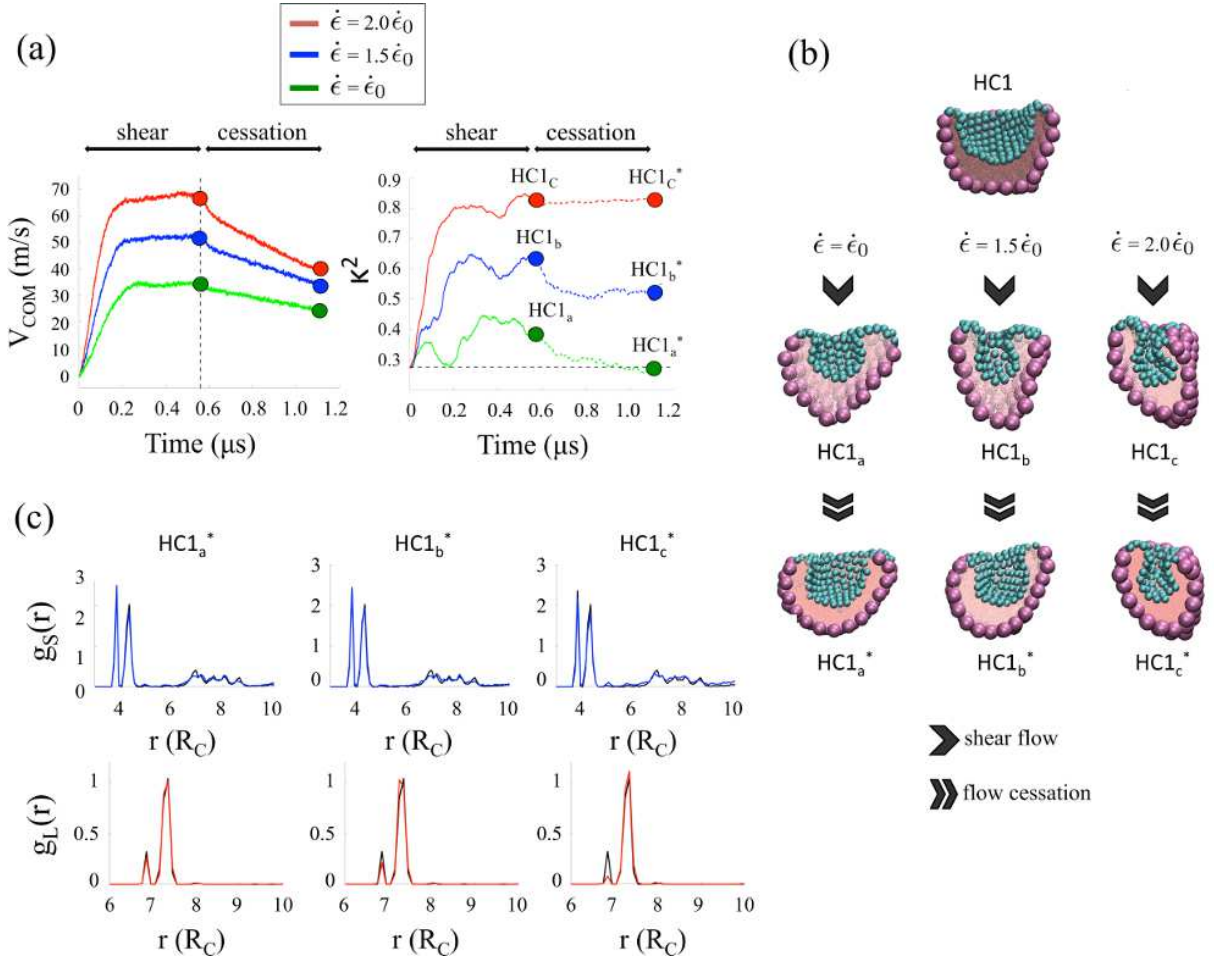


FIG. 2: **Dynamical response under shear flow.** (a) Temporal evolution of the velocity center of mass V_{COM} and the relative shape anisotropy κ^2 of HC1 subjected to shear flow and after abrupt shear cessation for three different values of the shear rate $\dot{\epsilon}$. The shear flow is continuously applied for a time duration $\Delta t \sim 0.6 \mu s$ before it is abruptly stopped and the structure relaxes for another $\Delta t \sim 0.6 \mu s$. (b) Representative snapshots of the armored nanodroplets obtained just before the flow cessation ($t \sim 0.6 \mu s$) and at the end of the simulation ($t \sim 1.2 \mu s$) are shown. Cyan and purple spheres represent the small and large Janus NPs, respectively. The detailed structure of the NPs is shown in Fig. S1a in the SI. Pink spheres represent water beads. The oil molecules surrounding the system are not shown for clarity. (c) Radial distribution function, $g_S(r)$ and $g_L(r)$, with r the distance between the center of the NPs, of small (blue) and large (red) NPs for HC1*_{a,b,c}. The corresponding radial distribution functions measured before the shear flow is applied (HC1) are shown in black color for comparison.

to the heterogeneity in NP size and surface coverage. In particular, the distribution of $\theta_C^{(L)}$ is similar to the one measured in the initial configuration, while the distributions of $\theta_C^{(S)}$ shows large variability, similar to the one measured in UC_S, during the buckling transition, originating from the difference in packing of the monolayer at the droplet interface, as shown in Fig. 1c.

Dynamical response under shear flow. Thereafter, we investigate the structural response of the buckled armored nanodroplets subjected to shear flow of the surrounding fluid using the SLLD algorithm [38, 39] coupled with Lee-Edwards periodic boundary conditions [40] (see Methods). We focus our analysis on HC1 whose structural morphology is more likely to yield bet-

ter loading of a probe load (cf. Fig. 1a). The minimum value for the shear rate, $\dot{\epsilon}_0 \sim 0.9 \text{ ns}^{-1}$, is set to the one for which the initial structure starts showing significant deformations. The system is first stressed under a constant shear rate, $\dot{\epsilon} = \alpha \times \dot{\epsilon}_0$, along the x -axis for a time duration $\Delta t \sim 0.6 \mu s$, with the parameter $\alpha = 1.0, 1.5, \text{ and } 2.0$. The length of the simulation is chosen sufficiently long for the velocity center of mass of the droplet, V_{COM} , to level off to a plateau whose value matches the one obtained from stationary velocity profile of laminar flow, $V_{COM} = \dot{\epsilon} \times L_y/2$, with $L_y \sim 77 \text{ nm}$ the size of the simulation box along the y -direction (cf. Fig. 2a). The flow is then abruptly halted and the dynamical stability of the nanodroplet is studied for a time duration $\Delta t \sim 0.6 \mu s$.

Representative snapshots of the structural morphology

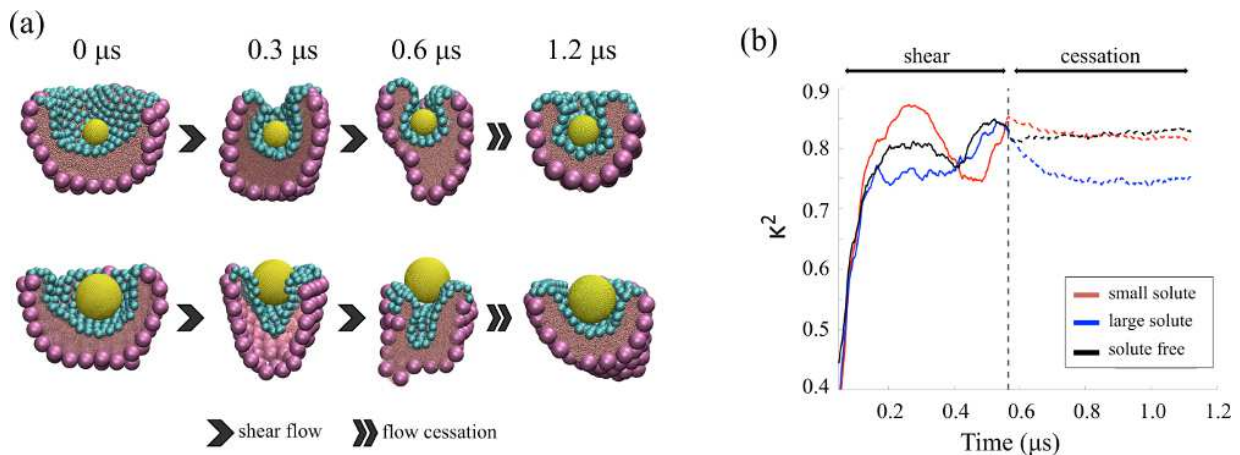


FIG. 3: **Encapsulation and release of load probe.** (a) Representative snapshots of the structural morphology of HC1 preliminary loaded with small (S) and large (L) hydrophobic spherical solute of diameter $d_S \sim 7.7$ nm (top panel) and $d_L \sim 15.4$ nm (bottom panel), respectively. Left, middle, and right panels correspond to the initial structure, and those obtained after $0.2 \mu s$ and $0.5 \mu s$, respectively. Cyan and purple spheres represent the small and large Janus NPs, respectively. The detailed structure of the NPs is shown in Fig. S1a in the SI. Pink and gold spheres represent water and solute beads. The oil molecules surrounding the system are not shown for clarity. (b) Representative temporal evolution of the relative shape anisotropy, κ^2 , of HC1 loaded with small and large solute, subjected to shear flow ($\dot{\epsilon} = 2 \times \dot{\epsilon}_0$) and after abrupt shear cessation. The shear flow is continuously applied for a time duration $\Delta t \sim 0.6 \mu s$ before it is abruptly stopped and the structure relaxes for another $\Delta t \sim 0.6 \mu s$. The evolution of κ^2 for the free system is shown for comparison.

of the armored nanodroplets obtained after $t \sim 0.6 \mu s$ and $t \sim 1.2 \mu s$, identified in Fig. 2a, are shown in Fig. 2b. Visual inspection shows different morphologies depending on the intensity of the shear rate and the relaxation of the system. The changes in structural morphology is quantitatively assessed with the measure of the relative shape anisotropy parameter, κ^2 , which reflects both the symmetry and dimensionality of the system [41, 42] (see Methods). As shown in Fig. 2a (right panel), we observe the increase of κ^2 at relatively short time until it levels off to a plateau when the velocity profile of the laminar fluid becomes stationary, and whose value depends on the intensity of the shear rate. In Figs. 2b and Fig. S3a in the SI, we observe the increase of κ^2 , associated with the elongation of the droplet along the deformation axis x and with the squeezing of the crater-like depression along the orthogonal z -direction. (HC1_{a,b,c}).

When the flow is abruptly halted at $t \sim 0.6 \mu s$, we observe either the relaxation of κ^2 towards its initial value (HC1_a^{*}) or the formation of long-lived anisotropic structure (HC1_{b,c}^{*}), depending on the intensity of $\dot{\epsilon}$. The specificity of the structural morphology of HC1_{b,c}^{*} can be explained by the formation of a jammed particle layer at the droplet interface, in qualitative agreement with recently reported experimental observations [43]. To do so, we assess the characteristics of the NP interfacial layer of HC1_{a,b,c}^{*} with the analysis of the three-phase contact angle distribution and the NP radial distribution function of small and large NPs. Within the range of shear rates considered in this work, $\theta_C^{(L)}$ follows a Gaussian distribution of mean $\mu_L \sim 87.2^\circ$ and standard deviation

$\sigma_L \sim 1.8^\circ$, similar to the one measured in both the initial and buckled configurations (cf. Fig. 1c). $\theta_C^{(S)}$, on the other hand, shows a skewed unimodal distribution with a central peak located at the same value as the one measured for both the initial and buckled configurations. The skewness of the distribution does not depend significantly on the intensity of the shear rate within the standard errors (cf. Fig. S3 in the SI).

Most importantly, the radial distribution functions, g_S and g_L , of small and large NPs, respectively, show different behaviours depending on the size of the NPs, as shown in Fig. 2c. Whereas g_S follows the same evolution as the one measured in HC1 before the shear rate is applied, the evolution of g_L reflects the local reorganisation of the layer made solely of large NPs at the droplet interface, as shown with the gradual decrease of its first peak associated with the first coordination sphere, eventually recovering the distribution observed in the initial spherical configuration shown in Fig. 1d.

Encapsulation and release of probe load. Our results so far allow us to address our second aim of investigating the dynamical response of the system under shear stress, when the buckled armored nanodroplet is preliminary loaded with a probe load, as shown in Fig. 3a. Then, we determine the ability of HC1_c to lead to the encapsulation or release of the solutes under flow conditions identical to those studied in the free configuration. We consider the largest shear rate, $\dot{\epsilon} = 2 \times \dot{\epsilon}_0 \sim 1.8 \text{ ns}^{-1}$, which shows the strongest structural deformation of the system, as shown in Figs. 2a (right panel). One small (S_S) and one large (S_L) spherical hydrophobic solutes

	free	S_S	S_L
$\langle \kappa^2 \rangle$	0.81 ± 0.02	0.79 ± 0.04	0.80 ± 0.05
$\delta\kappa^2$	$1.2\% \pm 0.3\%$	$4.4\% \pm 1.6\%$	$6.4\% \pm 4.5\%$

TABLE II: Estimation of the average value of κ^2 when the system reaches a stationary state under flow conditions, $\langle \kappa^2 \rangle$, and the relative change $\delta\kappa^2$ between the beginning and the end of the relaxation period. Uncertainties are determined by considering three replica of the systems, and calculating the standard error.

are considered, with radius $r_S^{(s)} \sim 4$ nm and $r_L^{(s)} \sim 8$ nm, respectively. The size of S_S and S_L is specifically chosen so that they can be preliminarily loaded in the crater-like depression formed at the interface of HC1, obtained after the last removal of water (cf Fig. 1a). S_S and S_L , however, differ in their ability to eventually fit or not in HC1_c when the shear stress is applied. The characteristics of the spherical solutes in the DPD framework are given in the Methods section.

The system is first stressed under constant shear rate along the x -axis for a time duration $\Delta t \sim 0.6 \mu\text{s}$, sufficiently long to observe the flow-assisted encapsulation or release of the small and large solutes, respectively. The flow is then abruptly halted and the relaxation of the system is studied for a time duration $\Delta t \sim 0.6 \mu\text{s}$. In Fig. 3a we show representative snapshots of the systems loaded with the two spherical solutes, S_S and S_L , at different simulation stages. When the solute is sufficiently small, the particle-laden interface folds inward under surface stress leading to the encapsulation of the solute. When the solute is sufficiently large, however, the crater-like depression cannot accommodate the solute when the system is stressed. Therefore, S_L is progressively expelled from the pocket following the narrowing and elongation of the nanodroplet. As the flow is abruptly halted, the armored nanodroplet relaxes its structural morphology, accommodating the solute load inside the residual pocket, regardless the size of the load.

The evolution of the structural morphology of the loaded nanodroplets is quantitatively assessed with the estimation of the relative shape anisotropy, κ^2 , as shown in Fig. 3b. In particular, we compare the average value of κ^2 in the stationary regime, *i.e.* $0.2 \mu\text{s} \leq t \leq 0.6 \mu\text{s}$, defined as $\langle \kappa^2 \rangle = \frac{1}{\Delta t} \int \kappa^2(t) dt$, along with the relative change $\delta\kappa^2 = \left| \kappa^2(t = 1.2 \mu\text{s}) - \kappa^2(t = 0.6 \mu\text{s}) \right| / \kappa^2(t = 0.6 \mu\text{s})$, measured between the beginning ($t = 0.6 \mu\text{s}$) and the end ($t = 1.2 \mu\text{s}$) of the relaxation period. As shown in Tab. II, the values of $\langle \kappa^2 \rangle$ estimated in the free and loaded configurations do not differ significantly within the standard errors, suggesting the pocket-like nanodroplet passively encapsulates or expels the small and large solutes, respectively, under the flow conditions and solute characteristics considered in this work. When the flow is abruptly halted, on the other hand, we observe

the relaxation of the system, which accommodates the solute load inside the residual pockets. During this process, the relaxation of the structural morphology of the loaded nanodroplets differs from the solute-free configuration, as quantified with the relative change $\delta\kappa^2$ in Tab. II, in qualitative agreement with the visual inspection in Fig. 3a.

Perspectives in delivery technology. The flow-assisted encapsulation and release of load probes in armored nanodroplets reported so far can be extended to systems of larger dimensions under conditions similar to those expected in the high-shear regime of spreading topical medication on the skin (such as creams and ointments) and the transport of targeted carriers in pathological alterations of the vascular system (such as venous or arterial thrombosis). These predictions would depend on the original dimension of the spherical droplet along with the initial NP surface coverage, and the NP dimension to droplet size ratio, which would affect the surface area to volume ratio of the system and the average surface pressure of the particle-laden interface [36], respectively.

To extend our results, the flow properties of the system are analyzed with two essential control parameters, *i.e.* the Weber number (We) and the Ohnesorge number (Oh), commonly used in microfluidic [44, 45] and droplet formation [46]. The Weber number, $We = \rho_o v^2 d_D / \gamma$, represents the ratio of the disrupting inertial force to the restorative surface tension force, where ρ_o and v are the density and the relative velocity of the ambient fluid (decane oil) and d_D and γ are the diameter and the interfacial tension of the droplet, respectively. The Ohnesorge number, $Oh = \mu_W / \sqrt{\rho_W \gamma d_D}$, represents the relative importance of the viscous force to the inertial and surface tension forces, where μ_W and ρ_W are the dynamics viscosity and the density of the water droplet, respectively. From the calculation of Oh , one can define the critical Weber number, $We_C = 12 (1 + 1.5 \times Oh^{0.74})$, which corresponds to the minimum Weber number for a droplet to exhibit breakup modes [47]. Given $\gamma \sim 51.7 \text{ mN.m}^{-1}$ the interfacial tension for a planar decane/water interface [23, 29], $\rho_W \sim 1000 \text{ kg.m}^{-3}$ and $\rho_o \sim 726 \text{ kg.m}^{-3}$ the density of water and decane oil, respectively, $v \sim 50 - 70 \text{ m.s}^{-1}$ the stationary velocity of the laminar flow (cf. Fig.3a), $\mu_W = 8.9 \times 10^{-4} \text{ Pa.s}$ the dynamics viscosity of water, and $d_D \sim 40$ nm the droplet diameter obtained from the measure of R_{GYR} (cf. Fig. 2a), we obtain $Oh \sim 0.6$, $We_C \sim 25$, and $We \sim 1.4 - 2.8$, indicating the armored droplets considered in the flow-assisted encapsulation and release processes are outside their breakup regime [48].

Now, based on the estimation of the Weber number, we first extend our predictions to the high-shear regime of spreading water-in-oil/oil-in-water emulsion-based products. Given the relation $v \sim \dot{\epsilon} \times L_{\perp}$ with L_{\perp} the dimension of the system orthogonal to the flow direction, we obtain $We \sim \rho_o \dot{\epsilon}^2 L_{\perp}^2 d_D / \gamma$. Considering the average

thickness of a cream $L_{\perp} \sim 1$ cm and representative shear rates $\dot{\epsilon} \sim 10^2 - 10^3$ s⁻¹ [49, 50], we obtain the characteristic dimension of the emulsion droplet $d_D \sim 1 - 100$ μ m, corresponding to the minimal droplet size to observe the encapsulation or release mechanism, in agreement with the range of characteristic droplet sizes commonly used in topical pharmaceutical products [50, 51].

Either by skin adsorption or others intake paths, targeted carriers can reach bloodstream as required. The complexity of the flow scenarios present in the circulatory system defies the full description of the behaviour of our model carrier once entering into the body. However, it is possible to put our predictions into perspective with the transport of our model carrier in the vascular subsystem, in particular in the pathological flow conditions encountered in venous or arterial thrombosis [52]. The fluid properties of the hepatic artery in non-pathological conditions, which is representative of a large artery, has a characteristic dimension $L_{\perp} \sim 5$ mm, and shear rate $\dot{\epsilon} \sim 500$ s⁻¹ [53]. A pathological flow, on the other hand, can be defined as where the blood reaches shear rates $\dot{\epsilon} > 5000$ s⁻¹, resulting, for example, from pathological clotting of blood within the lumen of a vessel [54]. Considering $\rho_{\text{blood}} \sim 1060$ kg.m⁻³ and $\gamma \sim 42$ mN.m⁻¹ as representative values of the average density and interfacial tension (against fluorocarbon) of the blood fluid [55], along with the narrowing of the pathological vessel $L_{\perp} \rightarrow L_{\perp}/2$, we obtain $d_D \sim 500$ nm for the minimal droplet dimension in the conditions of the hepatic artery with pathological alterations to observe the encapsulation or release mechanism. For comparison, we obtain $d_D \sim 10$ μ m for the minimal droplet dimension in the conditions of the normal hepatic artery, in the range of sizes characteristic of leucocyte and red blood cells [56]. As a result, the process of targeted-delivery of active-compounds (such as antithrombotic agents) can be selectively controlled with the size of the model nanocarrier.

Conclusions

The numerical simulations discussed above allowed us to unravel the interplay between the structural morphology of armored nanodroplets and the organisation of the NP interfacial network, when the volume of the system is reduced, in qualitative agreement with experimental observation [35]. We showed that finite-size NPs can strongly affect the droplet shape with the formation of *pocket-like* depressions, which can structurally favour the loading of a probe load. Eventually, our method would allow including specific interactions inside the formed cavity in order to mimic, for example, protein binding pockets or catalytic nanosurfaces.

The dynamical response of specifically designed *pocket-like* nanodroplets under different shear flow conditions exhibited the formation of long-lived anisotropic structures, characteristic of a jammed particle coverage at the liquid-liquid interface, associated with the dynamical rearrangement of the NP interfacial network. Most importantly, the ability of *pocket-like* nanodroplets to encapsulate or release spherical solute loads, located inside the crater-like depression, during their transport under shear-flow conditions was validated.

Our predictions on the flow-assisted encapsulation and release of load probes in armored nanodroplets were extended to systems in the micron scale encountered in pharmaceutical and cosmetic technology. Noticeably, we demonstrated that the mechanism reported in our work could be at play at larger scales, such as those encountered in the high-shear regime of spreading creams and ointments on the skin, and the transport of targeted carriers in pathological alterations of the vascular system. We put the physical properties of our model carrier into perspective within the conditions encountered in the pathological alteration of the hepatic artery, where the formation of a blood clot inside the blood vessel can obstruct the flow of blood through the circulatory system increasing the haemodynamic shear stress and the risk of bleeding complications. In particular, hepatic artery thrombosis can be a very serious complication of liver transplantation, with mortality in children which can be as high as 70% [57]. Hence, it is essential to develop distinctive means to control the process of targeted-delivery of antithrombotic agents in the vascular system.

The physical insights discussed here provide a deeper understanding on the potential role played by nanoparticle-stabilized emulsions in the biomimetic design of novel hybrid materials for targeted-oriented active load delivery. This information could be useful for a variety of applications including the design of pharmaceutical carriers for drug delivery and pathogen encapsulation, where knowledge of the rheological properties of the system must be quantitatively assessed.

Acknowledgements

F.S. acknowledges J. Reguera for fruitful suggestions and A. Striolo for useful discussions. Via our membership of the UKs HEC Materials Chemistry Consortium, which is funded by EPSRC (EP/L000202), this work used the ARCHER UK National Supercomputing Service (<http://www.archer.ac.uk>).

[1] Silva, H.; Cerqueira, M.; Vicente, A. Nanoemulsions for Food Applications: Development and Characterization.

- [2] Aziz, Z.; Mohd-Nasir, H.; Ahmad, A.; Setapar, S.; Peng, W.; Chuo, S.; Khatoon, A.; Umar, K.; Yaqoob, A.; Ibrahim, M. Role of Nanotechnology for Design and Development of Cosmeceutical: Application in Makeup and Skin Care. *Front. Chem.* **2019**, *7*, 739.
- [3] Rosenblum, D.; Joshi, N.; Tao, W.; Karp, J.; Peer, D. Progress and challenges towards targeted delivery of cancer therapeutics. *Nature Comm.* **2018**, *9*, 1410.
- [4] Pickering, S. CXCVI-Emulsions. *J. Chem. Soc.* **1907**, *91*, 2001–2021.
- [5] Frelichowska, J.; Bolzinger, M.-A.; Valour, J.-P.; Mouaziz, H.; Pelletier, J.; Chevalier, Y. Pickering W/O Emulsions: Drug Release and Topical Delivery. *Int. J. Pharm.* **2009**, *23*, 7–15.
- [6] Aparicio, R.; García-Celma, M.; Vinardell, M. P.; Mitjans, M. In vitro studies of the hemolytic activity of microemulsions in human erythrocytes. *J. Pharm. Biomed. Anal.* **2005**, *39*, 1063–7.
- [7] Chevalier, Y.; Bolzinger, M. Emulsions stabilized with solid nanoparticles: pickering emulsions. *Colloids Surfaces A: Physicochem. Eng. Aspects* **2013**, *439*, 23–34.
- [8] Shi, D.; Faria, J.; Pham, T.; Resasco, D. Enhanced Activity and Selectivity of Fischer-Tropsch Synthesis Catalysts in Water/Oil Emulsions. *ACS Catal.* **2014**, *4*, 1944–1952.
- [9] Faria, J.; Ruiz, M. P.; Resasco, D. Carbon Nanotube/Zelite Hybrid Catalysts for Glucose Conversion in Water/Oil Emulsions. *ACS Catal.* **2015**, *5*, 4761–4771.
- [10] Qu, Y.; Huang, R.; Qu, Q.; Su, R.; He, Z. Structural Insight into Stabilization of Pickering Emulsions with Fe₃O₄@SiO₂ Nanoparticles for Enzyme Catalysis in Organic Media. *Part. Part. Syst. Charact.* **2017**, *34*, 1700117.
- [11] Shen, X.; Bonde, J. S.; Kamra, T.; Bülow, L.; Leo, J.; Linke, D.; Ye, L. Bacterial Imprinting at Pickering Emulsion Interfaces. *Angew. Chem. Int. Ed.* **2014**, *53*, 10687–10690.
- [12] Horváth, B.; Balázs, V.; Varga, A.; Böszörményi, A.; Kocsis, B.; Horváth, G.; Széchenyi, A. Preparation, characterisation and microbiological examination of Pickering nano-emulsions containing essential oils, and their effect on *Streptococcus mutans* biofilm treatment. *Nature Sci. Rep.* **2019**, *9*, 16611.
- [13] Sicard, F.; Striolo, A. Numerical Analysis of Pickering Emulsion Stability: Insights from ABMD Simulations. *Faraday Discuss.* **2016**, *191*, 287–304.
- [14] Ortiz, D. G.; Pochat-Bohatier, C.; Cambedouzou, J.; Bechelany, M.; Miele, P. Current Trends in Pickering Emulsions: Particle Morphology and Applications. *Engineering* **2020**, *6*, 468–482.
- [15] Seemann, R.; Brinkmann, M.; Pfohl, T.; Herminghaus, S. Droplet based microfluidics. *Rep. Prog. Phys.* **2012**, *75*, 16601–2012.
- [16] Orellana, L. C.; Baret, J. Rapid Stabilization of Droplets by Particles in Microfluidics: Role of Droplet Formation. *Chem. System Chem.* **2019**, *1*, 16–24.
- [17] Groot, R.; Warren, P. Dissipative Particle Dynamics: Bridging the Gap between Atomistic and Mesoscopic Simulation. *J. Chem. Phys.* **1997**, *107*, 4423–4435.
- [18] Reguera, J.; Ponomarev, E.; Geue, T.; Stellacci, F.; Bresme, F.; Moglianetti, M. Contact Angle and Adsorption Energies of Nanoparticles at the Air-Liquid Interface Determined by Neutron Reflectivity and Molecular Dynamics. *Nanoscale* **2012**, *7*, 5665–5673.
- [19] Giner-Casares, J.; Reguera, J. Directed self-assembly of inorganic nanoparticles at air/liquid interfaces. *Nanoscale* **2016**, *8*, 16589–16595.
- [20] Binks, B.; Yin, D. Pickering emulsions stabilized by hydrophilic nanoparticles: in situ surface modification by oil. *Soft Matter* **2016**, *12*, 6858–6867.
- [21] Sicard, F.; Striolo, A. Buckling in Armored Droplet. *Nanoscale* **2017**, *9*, 8567–8572.
- [22] Sicard, F.; Striolo, A. In *Anisotropic Particle Assemblies*; Wu, N., Lee, D., Striolo, A., Eds.; Elsevier: Amsterdam, 2018; pp 167 – 200.
- [23] Sicard, F.; Toro-Mendoza, J.; Striolo, A. Nanoparticles Actively Fragment Armored Droplets. *ACS Nano* **2019**, *13*, 9498–9503.
- [24] Zhang, J.; Grzybowski, B.; Granick, S. Janus Particle Synthesis, Assembly, and Application. *Langmuir* **2017**, *33*, 6964–6977.
- [25] Agrawal, G.; Agrawal, R. Janus Nanoparticles: Recent Advances in Their Interfacial and Biomedical Applications. *ACS Appl. Nano Mater.* **2019**, *2*, 1738–1757.
- [26] Binks, B.; Lumsdon, S. Influence of Particle Wettability on the Type and Stability of Surfactant-Free Emulsions. *Langmuir* **2000**, *16*, 8622–8631.
- [27] Luu, X.-C.; Yu, J.; Striolo, A. Nanoparticles Adsorbed at the Water/Oil Interface: Coverage and Composition Effects on Structure and Diffusion. *Langmuir* **2013**, *29*, 7221.
- [28] Fan, H.; Resasco, D.; Striolo, A. Amphiphilic Silica Nanoparticles at the Decane-Water Interface: Insights from Atomistic Simulations. *Langmuir* **2011**, *27*, 5264–5274.
- [29] Fan, H.; Striolo, A. Nanoparticle Effects on the Water-Oil Interfacial Tension. *Phys. Rev. E* **2012**, *86*, 051610.
- [30] Arnaudov, L.; Cayre, O.; Stuart, M. C.; Stoyanov, S.; Paunov, V. Measuring the three-phase contact angle of nanoparticles at fluid interfaces. *Phys. Chem. Chem. Phys.* **2010**, *12*, 328–331.
- [31] Binks, B.; Fletcher, P. Pickering Emulsions Stabilized by Monodisperse Latex Particles: Effects of Particle Size. *Langmuir* **2001**, *16*, 21–41.
- [32] Jiang, S.; Granick, S. Janus balance of amphiphilic colloidal particles. *J. Chem. Phys.* **2007**, *127*, 161102.
- [33] Khedr, A.; Striolo, A. Self-assembly of mono- and poly-dispersed nanoparticles on emulsion droplets: antagonistic vs. synergistic effects as a function of particle size. *Phys. Chem. Chem. Phys.* **2020**, *22*, 22662.
- [34] Wang, D.; Yordanov, S.; Paroor, H.; Mukhopadhyay, A.; Li, C.; Butt, H.; Koynov, K. Probing Diffusion of Single Nanoparticles at Water–Oil Interfaces. *Small* **2011**, *7*, 3502–3507.
- [35] Datta, S.; Shum, H.; Weitz, D. Controlled Buckling and Crumpling of Nanoparticle-Coated Droplets. *Langmuir Lett.* **2010**, *26*, 18612–18616.
- [36] Gu, C.; Botto, L. Buckling vs. particle desorption in a particle-covered drop subject to compressive surface stresses: a simulation study. *Soft Matter* **2018**, *14*, 711.
- [37] Basavaraj, M.; Fuller, G.; Fransaer, J.; Vermant, J. Packing, Flipping, and Buckling Transitions in Compressed Monolayers of Ellipsoidal Latex Particles. *Langmuir* **2006**, *22*, 6605–6612.
- [38] Evans, D. J.; Morriss, G. P. Non-Newtonian molecular dynamics. *Comput. Phys. Rep.* **1984**, *1*, 297.
- [39] Evans, D.; Morriss, G. Nonlinear-response theory for steady planar Couette flow. *Phys. Rev. A* **1984**, *30*, 1528.
- [40] Lees, A.; Edwards, S. F. The computer study of transport

- processes under extreme conditions. *J. Phys. C* **1972**, *5*, 1921.
- [41] Vymetal, J.; Vondrášek, J. Gyration- and Inertia-Tensor-Based Collective Coordinates for Metadynamics. Application on the Conformational Behavior of Polyalanine Peptides and Trp-Cage Folding. *J. Phys. Chem. A* **2011**, *115*, 11455–11465.
- [42] Arkin, H.; Janke, W. Gyration tensor based analysis of the shapes of polymer chains in an attractive spherical cage. *J. Chem. Phys.* **2013**, *138*, 054904.
- [43] Kaganyuk, M.; Mohraz, A. Shear-induced deformation and interfacial jamming of solid-stabilized droplets. *Soft Matter* **2020**, *16*, 4431.
- [44] Hall, S.; Pacek, A.; Kowalski, A.; Cooke, M.; Rothman, D. The effect of scale and interfacial tension on liquid–liquid dispersion in in-line Silverson rotor–stator mixers. *Chem. Engineering Research Design* **2013**, *91*, 2156–2168.
- [45] Xu, Z.; Wang, T.; Che, Z. Droplet deformation and breakup in shear flow of air. *Phys. Fluids* **2020**, *32*, 052109.
- [46] Roas-Escalona, N.; Williams, Y. O.; Cruz-Barrios, E.; Toro-Mendoza, J. Intertwining Roles of the Disperse Phase Properties during Emulsification. *Langmuir* **2018**, *34*, 6480–6488, PMID: 29758983.
- [47] Gelfand, B. Droplet Breakup Phenomena in Flows with Velocity Lag. *Progress Energy Combustion Sci.* **1996**, *22*, 201–265.
- [48] Derby, B. Inkjet Printing of Functional and Structural Materials: Fluid Property Requirements, Feature Stability, and Resolution. *Annu. Rev. Mater. Res.* **2010**, *40*, 395–414.
- [49] Walicka, A.; Falicki, J.; Iwanowska-Chomiak, B. Rheology of drugs for topical and transdermal delivery. *Int. J. of Applied Mechanics and Engineering* **2019**, *24*, 179–198.
- [50] Simoes, A.; Veiga, F.; Vitorino, C. Progressing Towards the Sustainable Development of Cream Formulations. *Pharmaceutics* **2020**, *12*, 647.
- [51] Lu, G.; Gao, P. In *Handbook of Non-Invasive Drug Delivery Systems*; Kulkarni, V. S., Ed.; Personal Care & Cosmetic Technology; William Andrew Publishing: Boston, 2010; pp 59 – 94.
- [52] Esmon, C. Basic Mechanisms and Pathogenesis of Venous Thrombosis. *Blood Rev.* **2009**, *23*, 225–229.
- [53] Sakariassen, K.; Orning, L.; Turitto, V. The impact of blood shear rate on arterial thrombus formation. *Future Sci. OA* **2015**, *1*, FSO30.
- [54] Herbig, B.; Yu, X.; Diamond, S. Using microfluidic devices to study thrombosis in pathological blood flows. *Biomicrofluidics* **2018**, *12*, 042201.
- [55] Mottaghy, K.; Hahn, A. Interfacial tension of some biological fluids: A comparative study. *J. Clin. Chem. Clin. Biochem.* **1981**, *19*, 267–271.
- [56] Phillips, R.; Kondev, J.; Theriot, J. *Physical Biology of the Cell*; Garland Science, Taylor & Francis Group, 2008.
- [57] Acharya, S. S.; Sarangi, S. N. In *Lanzkowsky’s Manual of Pediatric Hematology and Oncology (Sixth Edition)*, sixth edition ed.; Lanzkowsky, P., Lipton, J. M., Fish, J. D., Eds.; Academic Press: San Diego, 2016; pp 279 – 333.
- [58] Groot, R.; Warren, P. Dissipative Particle Dynamics: Bridging the Gap between Atomistic and Mesoscopic Simulation. *J. Chem. Phys.* **1997**, *107*, 4423–4435.
- [59] Plimpton, S. Fast Parallel Algorithms for Short-Range Molecular Dynamics. *J. Comput. Phys.* **1995**, *117*, 1–19.
- [60] Groot, R.; Rabone, K. Mesoscopic Simulation of Cell Membrane Damage, Morphology Change and Rupture by Nonionic Surfactants. *Biophys. J.* **2001**, *81*, 725.
- [61] Calvaresi, M.; Dallavalle, M.; Zerbetto, F. Wrapping Nanotubes with Micelles, Hemimicelles, and Cylindrical Micelles. *Small* **2009**, *5*, 2191–2198.
- [62] X-C.Luu.; Yu, J.; Striolo, A. Ellipsoidal Janus Nanoparticles Adsorbed at the Water-Oil Interface: some evidence of emergent behavior. *J. Phys. Chem. B* **2013**, *117*, 13922–13929.
- [63] Partington, J.; R.F.Hudson.; Bagnall, K. Self-Diffusion of Aliphatic Alcohols. *Nature* **1952**, *169*, 583.
- [64] Warren, P. Vapor-liquid coexistence in many-body dissipative particle dynamics. *Phys. Rev. E: Stat. Phys., Plasmas, Fluids, Relat. Interdiscip. Top.* **2003**, *68*, 066702.
- [65] Fan, H.; Striolo, A. Mechanistic Study of Droplets Coalescence in Pickering Emulsions. *Soft Matter* **2012**, *8*, 9533–9538.
- [66] Solc, K. Shape of a Random-Flight Chain. *J. Chem. Phys.* **1971**, *55*, 335.

Methods

Mesoscopic framework. The Dissipative Particle Dynamics (DPD) simulation method [58] is implemented within the simulation package LAMMPS [59]. In the DPD simulations, a particle represents a cluster of atoms rather than an individual atom. These particles interact with each other through soft particle-particle interactions. The movement of the particle can be realized by solving the Newton’s equation of motion

$$\frac{d\mathbf{r}_i}{dt} = \mathbf{v}_i, \quad m_i \frac{d\mathbf{v}_i}{dt} = \mathbf{F}_i, \quad (1)$$

where m_i , \mathbf{r}_i , \mathbf{v}_i , and \mathbf{F}_i denote the mass, position, velocity, and total force acting on the i th particle, respectively. The total force \mathbf{F}_i is divided into three parts, the conservative force (\mathbf{F}_{ij}^C), dissipative force (\mathbf{F}_{ij}^D), and random force (\mathbf{F}_{ij}^R), and defined as $\mathbf{F}_i = \sum_{j \neq i} (\mathbf{F}_{ij}^C + \mathbf{F}_{ij}^D + \mathbf{F}_{ij}^R)$ with

$$\mathbf{F}_{ij}^C = a_{ij} \sqrt{\omega(r_{ij})} \hat{\mathbf{r}}_{ij}, \quad (2)$$

$$\mathbf{F}_{ij}^D = -\Gamma \omega(r_{ij}) (\hat{\mathbf{r}}_{ij} \cdot \mathbf{v}_{ij}) \hat{\mathbf{r}}_{ij}, \quad (3)$$

$$\mathbf{F}_{ij}^R = \sigma \sqrt{\omega(r_{ij})} \theta_{ij} \hat{\mathbf{r}}_{ij} \quad (4)$$

where $\mathbf{r}_{ij} = \mathbf{r}_i - \mathbf{r}_j$, $r_{ij} = |\mathbf{r}_{ij}|$, $\hat{\mathbf{r}}_{ij} = \mathbf{r}_{ij}/r_{ij}$, and $\mathbf{v}_{ij} = \mathbf{v}_i - \mathbf{v}_j$. The weight function $\omega(r_{ij})$ equals to $(1 - r_{ij}/R_c)^2$ with a cut-off distance R_c . a_{ij} , Γ , σ , and θ_{ij} are the repulsive parameter, friction coefficient, noise amplitude, and Gaussian random variable, respectively. To keep the temperature of the system constant, Γ and σ satisfy the fluctuation-dissipation theorem as $\sigma^2 = 2\Gamma k_B T$, where k_B and T are the Boltzmann and the absolute temperature, respectively.

The system simulated here is composed of water, oil (decane), nanoparticles (NPs) and solute molecules.

Following previous work [13, 21, 23, 27], we choose the degree of coarse graining $N_m = 5$ with the understanding that one "water bead" (w) represents 5 water molecules. Within this assumption, the volume of each bead is $V_{\text{bead}} \approx 150 \text{ \AA}^3$. The scaled density is set to $\rho = 3$ beads/ R_c^3 , where R_c is the DPD cutoff distance given as $R_c = \sqrt[3]{\rho V_{\text{bead}}} \approx 0.766$ nm. The scaled mass of each bead (oil, water, solute molecule, and NP beads) was set to 1. One decane molecule is modeled as two "oil beads" (o) connected by one harmonic spring of length $0.72 R_c$ and spring constant $350 k_B T / R_c$ [60]. The size of the triclinic simulation box (initially orthogonal) is $L_x \times L_y \times L_z \equiv 200 \times 100 \times 100 R_c^3$, where L_x (respectively L_y and L_z) is the box length along the X (respectively Y and Z) direction. Periodic boundary conditions are applied in all three directions. The solute molecules and the NPs are modelled as hollow rigid spheres, as already described in previous work [13, 21, 23, 27]. The hydrophobic solute molecules are made of nonpolar DPD beads, whereas the NPs contain polar (p) and nonpolar (ap) DPD beads on their surface [61]. One DPD bead was placed at the NP and solute molecule centers for convenience, as described elsewhere [27, 62]. All types of beads in our simulations have reduced mass of 1. We maintain the surface bead density on the NPs and solute molecule sufficiently high to prevent other DPD beads (either decane or water) from penetrating the NPs and solute molecules [62].

The interaction parameters shown in Table III are used here. These parameters are adjusted to reproduce selected atomistic simulation results, as explained in prior work [27]. The interaction parameters between NP polar and nonpolar beads, as well as solute molecule beads, are adjusted to ensure that NPs/NPs and NPs/solute are able to assemble and disassemble without yielding permanent dimers at the water/oil interface [27]. The scaled temperature was set to 1, equivalent to 298.73 K. The time step $\delta t = 0.03 \times \tau$ was used to integrate the equations of motion, where τ is the DPD time constant. As demonstrated by Groot and Rabone [60], the time constant of the simulation can be gauged by matching the simulated self-diffusion of water, D_{sim} , with the the experimental water self-diffusion coefficient, $D_{\text{water}} = 2.43 \times 10^{-5} \text{ cm}^2/\text{s}$ [63], calculated as $\tau = \frac{N_m D_{\text{sim}} R_c^2}{D_{\text{water}}}$, as shown in previous work [27]. When $a_{w-w} = 131.5 k_B T / R_c$, this results in a time step $\delta t = 5.6$ ps.

While the DPD framework satisfies the Navier-Stokes equations in the continuum limit [58], the traditional DPD algorithm cannot reproduce the vapour-liquid coexistence of water at the droplet interface [64]. This is due to the DPD conservative force, which determines the thermodynamics of the DPD system and yields the equation of state (EOS) [58]

$$p = \rho k_B T + \alpha a \rho^2, \quad (5)$$

where p is the pressure, ρ is the number density of the

	w	o	ap	p	s
w	131.5	198.5	178.5	110	670
o		131.5	161.5	218.5	161.5
ap			450	670	450
p				450	670
s					131.5

TABLE III: DPD interaction parameters expressed in $k_B T / R_c$ units. Symbols w , o , ap , p , and s stand for water beads, oil beads, NP nonpolar beads, NP polar beads, and solute beads, respectively.

DPD beads, a is the repulsion strength, and α is a fitting parameter equal to 0.101 ± 0.001 in DPD reduced units [58]. As shown by Warren in Ref. [64], The DPD system is unstable for $a < 0$, so one is restricted to $a \geq 0$ and therefore to strictly repulsive (conservative) interactions. This implies that calculations such as the vapor-liquid coexistence and free-surface simulations cannot be attempted. This can be adjusted by considering higher order terms of the density, ρ , in Eq. (5), *i.e.* making the conservative force in Eq. (2) density dependent [64].

Nonequilibrium simulation. To simulate the response of the system subjected to an homogeneous shear flow, we employ the SLLOD algorithm [38, 39] coupled with the Lee-Edwards periodic boundary conditions [40], as implemented in the simulation package LAMMPS [59]. The SLLOD algorithm modifies the equations of motion in Eq. 1 as:

$$\frac{d\mathbf{x}_i}{dt} = \mathbf{v}_i + \mathbf{e}_x \dot{\epsilon} r_{i,y}, \quad (6)$$

$$m_i \frac{d\mathbf{v}_i}{dt} = \mathbf{F}_i - m_i \mathbf{e}_x \dot{\epsilon} v_{i,y}, \quad (7)$$

where $\dot{\epsilon} = \partial v_x / \partial r_y$ is the shear rate of the external flow and $\mathbf{e}_{x,y}$ are the unit vectors along the x and y directions, respectively. The velocity of the i th particle is divided into two parts, that is, the peculiar velocity \mathbf{v}_i representing the random thermal motions and the shear flow velocity $\mathbf{e}_x \dot{\epsilon} v_{i,y}$ relating to the external disturbance strength. Specifically, we impose a linear velocity profile in the x direction with a constant gradient in the y direction, keeping the density of the system constant, by changing the xy -tilt factor, T_{xy} , of the triclinic simulation box at a constant shear rate, $\dot{\epsilon}$, as

$$T_{xy}(t) = T_{xy}^{(0)} + \dot{\epsilon} L_0 \Delta t. \quad (8)$$

In Eq. 8, $T_{xy}^{(0)}$ and L_0 are the initial tilt factor and the original length of the box perpendicular to the shear direction. This can be related to the shear stress of the external shear flow $\tau_s = \mu \dot{\epsilon}$, with μ the dynamic viscosity of the continuous phase.

Three phase contact angle. To estimate the three phase contact angle, θ_C , for the NPs on the droplets we calculate the fraction of the spherical NP surface area that is wetted by water [65],

$$\theta_C = 180 - \arccos\left(1 - \frac{2A_w}{4\pi R^2}\right), \quad (9)$$

where A_w is the area of the NP surface that is wetted by water and R is the radius of the NP. The ratio $A_w/4\pi R^2$ is obtained by dividing the number of NP surface beads (ap or p), which are wetted by water, by the total number of beads on the NP surface. One surface bead is wet by water if a water bead is the solvent bead nearest to it. One standard deviation from the average is used to estimate the statistical uncertainty.

Interfacial tension. The interfacial tension γ at the water/oil interface as a function of the NP surface coverage Φ is calculated as [27, 29]

$$\gamma = \left\langle P_{zz} - \frac{P_{xx} + P_{yy}}{2} \right\rangle \frac{L_z}{2}. \quad (10)$$

In Eq. 10, P_{ij} is the ij element of the pressure tensor, L_z is the simulation box length in the z dimension, and the angular brackets denote the ensemble average.

Self-diffusion coefficient. To characterize the self-diffusion coefficient of the NPs at the water/oil interface, we estimate the mean squared displacement (MSD) of a single NP adsorbed at a planar interface parallel to the $x-y$ plane. For each particle size, the simulated diffusion coefficient is estimated according to

$$D_{x-y} = \frac{1}{4} \left\langle \frac{|r_i(t) - r_i(0)|^2}{t} \right\rangle \quad (11)$$

where $r_i(t)$ is the position of particle i at time t on the plane of the interface.

Gyration tensor. To measure the evolution of the structural morphology of the emulsion droplet, we estimate the principal components of the gyration tensor [13, 41, 66], which allow the evaluation of the overall shape of the system and reveal its symmetry. Considering the definition for the gyration tensor,

$$\mathcal{T}_{GYR} = \frac{1}{N} \begin{bmatrix} \sum x_i^2 & \sum x_i y_i & \sum x_i z_i \\ \sum x_i y_i & \sum y_i^2 & \sum y_i z_i \\ \sum x_i z_i & \sum y_i z_i & \sum z_i^2 \end{bmatrix}, \quad (12)$$

where the summation is performed over N atoms and the coordinates x , y , and z are related to the geometrical center of the atoms, one can define a reference frame where \mathcal{T}_{GYR} can be diagonalized:

$$\mathcal{T}_{GYR}^{diag} = \begin{bmatrix} S_1^2 & 0 & 0 \\ 0 & S_2^2 & 0 \\ 0 & 0 & S_3^2 \end{bmatrix}. \quad (13)$$

In Eq. 13, we follow the convention of indexing the eigenvalues according to their magnitude, *i.e.* $S_1^2 > S_2^2 > S_3^2$. We define the radius of gyration $R_{GYR}^2 \equiv S_1^2 + S_2^2 + S_3^2$ and the relative shape anisotropy $\kappa^2 = \frac{3}{2} \frac{S_1^4 + S_2^4 + S_3^4}{(S_1^2 + S_2^2 + S_3^2)^2} - \frac{1}{2}$, and we calculate R_{GYR} and κ^2 using the centers of the water beads.

Computational design of armored nanodroplets as nanocarriers for encapsulation and release under flow conditions

Supporting Information

Nanoparticle characteristics

Following previous work [13, 21, 23, 27–29], the nanoparticles (NPs) are specifically designed to represent Janus silica NPs (particles whose surface shows two distinct wetting properties) at the decane/water interface. The NPs are modelled as hollow rigid spheres with two different diameters, $d_S \sim 3R_c$ and $d_L \sim 6R_c$ for small and large NPs, respectively, with $R_c \sim 0.766$ nm the DPD cutoff distance. Each NP contains polar (p) and nonpolar (ap) DPD beads on its surface and one DPD bead is placed at the NP center for convenience, as shown in Fig. S1a. Hollow models have been used in the literature to simulate NPs, and hollow NPs can also be synthesized experimentally [61]. All types of beads in our simulations have reduced mass of 1. To cover small and large NPs, 108 and 432 beads are required, respectively, yielding a surface density of ≈ 3.8 beads per R_c^2 on the NP surface [29]. The total number of beads on one NP surface is chosen such that the surface bead density be sufficiently high to prevent other DPD beads (either decane or water) from penetrating the NPs (which would be unphysical), as it has already been explained elsewhere [62]. We use the same surface density for the hydrophobic spherical probe load.

The NP-solvent interaction parameters in the DPD framework, given in the Methods section in the main text, were originally parametrized to reproduce the three-phase contact angle, $\theta_c \sim 85.3^\circ \pm 1.9^\circ$, obtained via atomistic molecular dynamics (MD) simulations for one silica Janus NP of diameter $\sim 2R_c$ at the decane/water interface, as explained in previous work [27–29]. In our case, we check that the three-phase contact angles for small and large NPs, $\theta_S \sim 84.1^\circ \pm 2.7^\circ$ and $\theta_L \sim 86.8^\circ \pm 1.1^\circ$, respectively, as shown in Fig. S1b, are in qualitative agreement, within the standard errors, with experimental observations [30]. From the error bars measured, we observe that the small NPs are more sensitive to thermal fluctuations at the interface compared to the large ones, characteristic of the increase of the adsorption energy with the particle radius [31–33].

To evaluate the diffusion of the small and large NPs at the water/oil interface, we estimate the mean squared displacement (MSD) of a single NP adsorbed at a planar water/oil interface parallel to the $x - y$ plane for increasing simulation lagtime, as shown in Fig. S1c. For each particle size, the MSD is averaged over 5 replicas conducted for $1 \mu\text{s}$ each, and the simulated diffusion coefficient is estimated accordingly (see Methods section in the main text). We measure $D_S \sim 4.7 \pm 3.1 \times 10^{-7} \text{ cm}^2 \text{ s}^{-1}$ and $D_L \sim 1.8 \pm 0.7 \times 10^{-7} \text{ cm}^2 \text{ s}^{-1}$, for small and large NPs, respectively. In particular, large NPs are less diffusive than smaller ones, in qualitative agreement with simulations [33] and experimental observations [34].

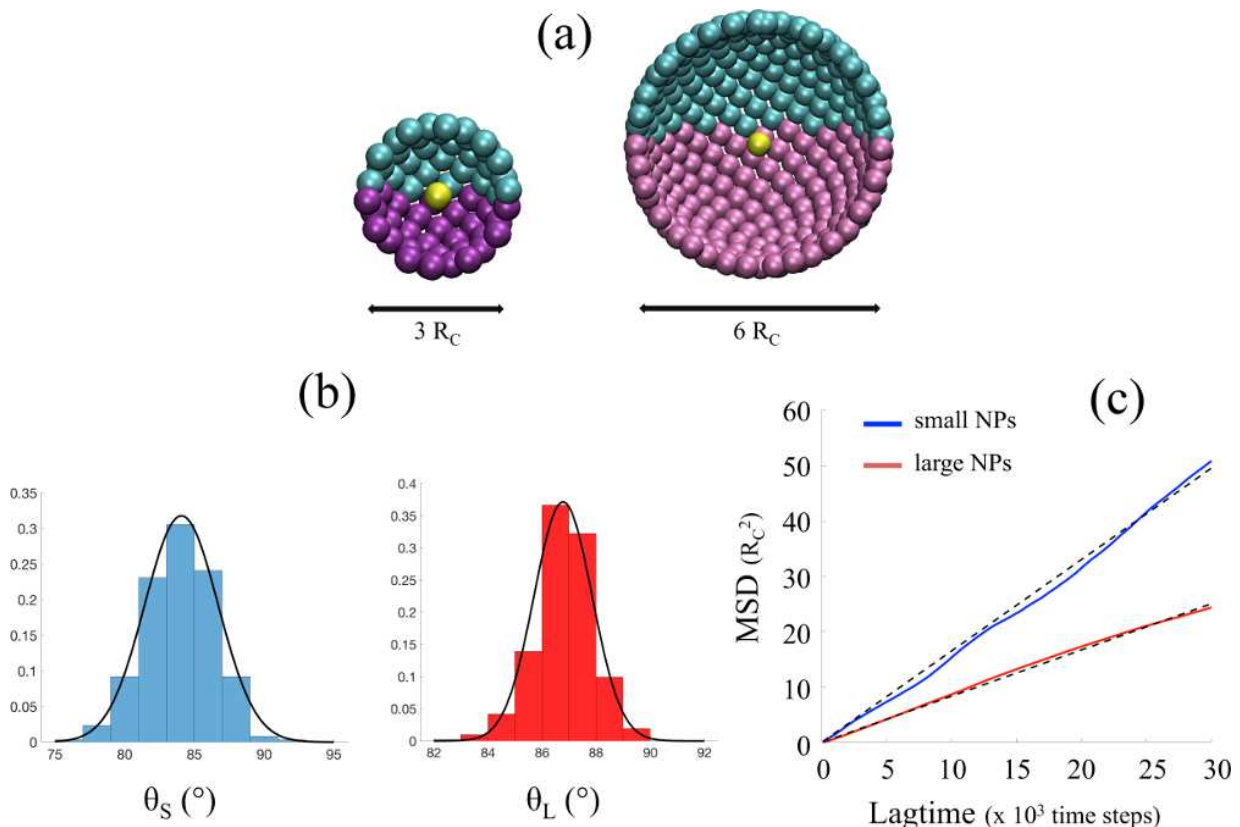


FIG. S1: (a) Cross sectional view of the small (left panel) and large (right panel) spherical NPs simulated in this work. Cyan, purple and gold spheres represent the nonpolar (ap), polar (p), and NP center beads, respectively. Small and large NPs are covered with 108 and 432 beads, respectively, corresponding to a surface density of ~ 3.8 beads per R_C^2 on the NP surface. The fractions of nonpolar and polar beads on the NP surface are identical. (b) Probability distributions of the three-phase contact angles θ_S and θ_L for small (S) and large (L) NPs, respectively. The probability distributions is fitted with Gaussian distributions of means $\mu_S \sim 84.1^\circ$ and $\mu_L \sim 86.8^\circ$, and standard deviations $\sigma_S \sim 2.7^\circ$ and $\sigma_L \sim 1.1^\circ$, as shown with continuous lines. (c) MSD as a function of simulation lagtime for small and large NPs measured at the water/oil planar interface.

Formation of pocket-like structures

The number of water beads constituting the initial water-in-oil emulsion droplets is fixed to $N_W \approx 3 \times 10^5$. At the beginning of each simulation, the solvent (oil) beads are uniformly distributed within the simulation box. One water droplet of radius $\approx 32 R_C$ is generated by replacing the oil beads with water beads within the volume of the spherical surface. A number of spherical NPs are placed randomly at the water-decane interface with their polar (nonpolar) part in the water (oil) phase to achieve the desired water-decane interfacial area per NP. The initial configuration obtained is simulated for 10^6 timesteps in order to relax the density of the system and the contact angle of the NPs on the droplet. The system pressure and the three-phase contact angle distributions converged after 5000 simulation steps. Then, we let the system run for an additional 2×10^6 timesteps to generate two new initial configurations, which allows us to test the reproducibility of the simulations.

To study the surface mechanical instabilities and the collapse mechanisms responsible for the formation of the crater-like depressions at the droplet interface, we follow the numerical protocol discussed by Sicard et al. in previous work [21]. The surface area of the droplets is slowly diminished, pumping randomly a constant proportion, *i.e.* 10 percent, of water molecules out of the droplet and letting the system pressure and the three-phase contact angle distribution equilibrate at constant density. By slowly, we mean we do not create any hollow volume in the droplet that would strongly drive the system out-of-equilibrium. Doing so, the three-phase contact angle distribution of the NPs evolves sufficiently smoothly when the droplet buckles and becomes nonspherical, thereby preventing particles to be artifactually released. This numerical protocol is comparable to a solubilization experiment, where the dispersed phase is slightly soluble in the continuous phase [35]. By adding a fixed amount of unsaturated continuous phase, the volume of the droplets can then be controllably reduced.

To study quantitatively the transition from spherical shrinking to buckling in the uniformly covered droplets, UC_S and UC_L , we follow the evolution of the radial distribution functions, $g_S(r)$ and $g_L(r)$, with r the distance between the center of the NPs, along with the distributions of the three-phase contact angles, θ_S and θ_L , of small and large NPs, respectively. In Fig. S2a, we show the evolution of $g(r)$, as a function of the dimensionless parameter ΔN_W defined in the main text, for UC_S (blue) and UC_L (red). Unlike UC_S where the first peak in $g(r)$ is already present for $\Delta N_W \sim 0.8$ and increases significantly when ΔN_W decreases, we observe the apparition of the first peak in $g(r)$ for UC_L at a later stage ($\Delta N_W \sim 0.72$). This peak increases significantly slower when ΔN_W decreases. This behaviour is representative of the difference in NP interfacial packing as a function of the NP size, with a transition from spherical shrinking to buckling happening when the NP monolayer becomes close to its maximum packing. When the volume of UC_S and UC_L is reduced, $\theta_C^{(S)}$ and $\theta_C^{(L)}$ uniformly evolve from a Gaussian to a skewed unimodal distribution, as shown in Fig. S2b for UC_L , in line with previous work [21]. When the volume of HC_1 or HC_2 is reduced, on the other hand, we observe significant differences in the evolution of the distributions of $\theta_C^{(S)}$ and $\theta_C^{(L)}$, due to heterogeneity in NP size and surface coverage, as shown in Fig. S2c. In particular, the distribution of $\theta_C^{(L)}$ remains similar to the Gaussian distribution observed in the initial configuration (continuous line), while the distributions of $\theta_C^{(S)}$ shows larger variability, characterized with the increase of the asymmetry of the distribution towards lower values of θ_S .

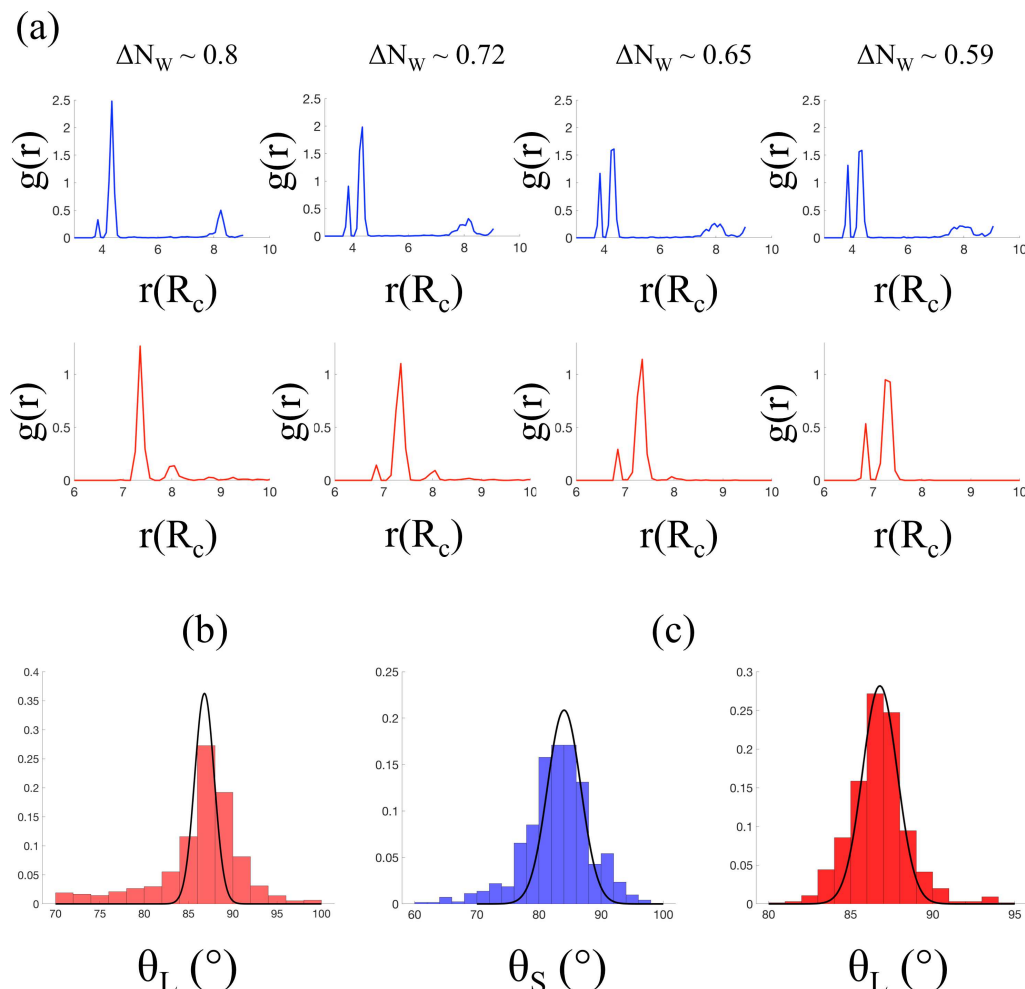


FIG. S2: (a) Evolution of the NP radial distribution function, $g(r)$, as a function of the dimensionless parameter ΔN_W , defined in the main text, when the droplet is uniformly covered with small (top panel) and large (bottom panel) NPs. (b) Probability distribution of the three-phase contact angle of large NPs, θ_L , at the interface of UC_L , when $\Delta N_W \sim 0.35$. The initial Gaussian distribution, fitted with continuous line, is shown for comparison. (c) Probability distributions of the three-phase contact angle of θ_S and θ_L , for small and large NPs, respectively, at the interface of HC_1 , when $\Delta N_W \sim 0.35$. The initial Gaussian distributions, fitted with continuous lines, are shown for comparison.

Evolution of the structural morphology of the droplets under flow conditions

As explained in details in the main text and the Methods section, we investigate the dynamical response of the buckled armored nanodroplets HC_1 subjected to shear flow of the surrounding fluid, using the SLLOD algorithm [38, 39] coupled with Lee-Edwards periodic boundary conditions [40]. The changes in the structural morphology of the system are characterized with the elongation of the nanodroplet along the deformation axis x , and the squeezing of the crater-like depression along the orthogonal z -direction, as shown in Fig. S3a. In Fig. S3b, we show the probability distribution of the three-phase contact angle, $\theta_C^{(S)}$, for small NPs, at the interface of the structures $\text{HC1}_{a,b,c}$ defined in the main text. Within the range of shear rates considered in this work, $\theta_C^{(S)}$ shows a skewed unimodal distribution with a central peak located at the same value as the one measured for both the initial and buckled configurations (shown with continuous lines).

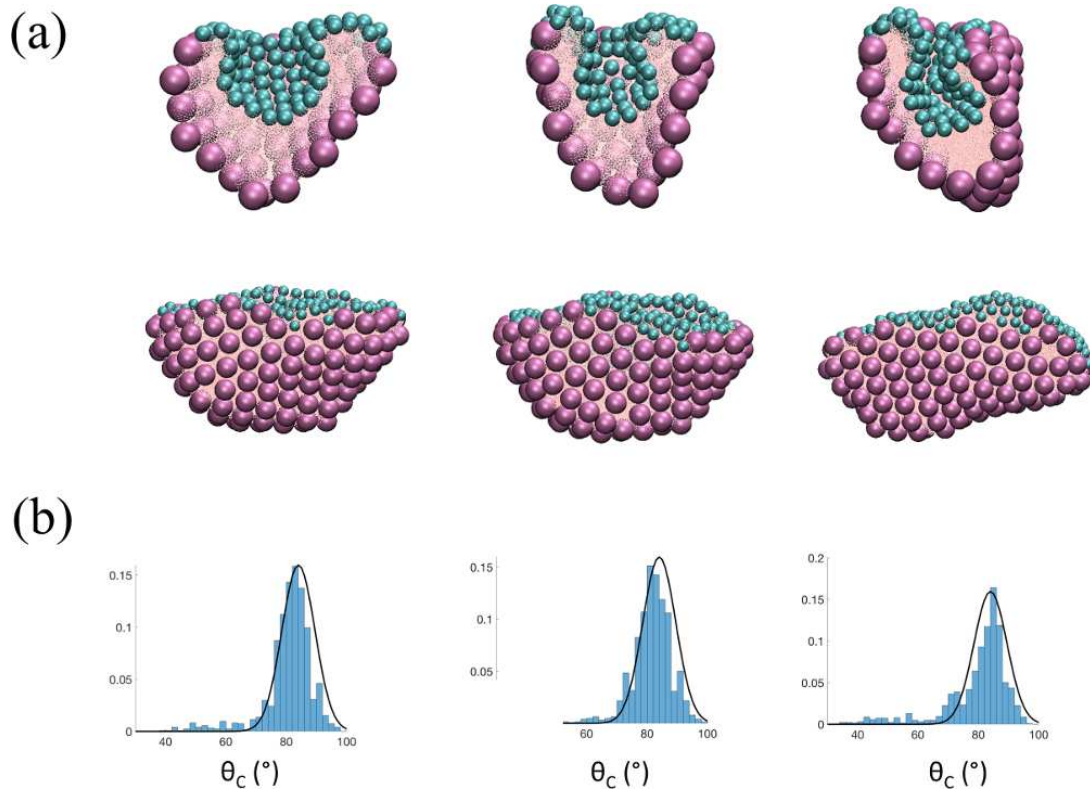


FIG. S3: (a) Representative cross-view (top) and side-view (bottom) of $\text{HC1}_{a,b,c}$ (from left to right) obtained after the relaxation of the system ($t \sim 1.2 \mu\text{s}$). Cyan and purple spheres represent the small and large Janus NPs, respectively. Pink spheres represent water beads. The oil molecules surrounding the system are not shown for clarity. (b) Corresponding distributions of the three-phase contact angle, $\theta_C^{(S)}$, for small NPs, at the interface of the structures $\text{HC1}_{a,b,c}$.